International Journal of Minerals, Metallurgy and Materials
Volume 23, Number 8, August 2016, Page 981
DOI: 10.1007/s12613-016-1315-z

Pseudo-*in-situ* stir casting: a new method for production of aluminum matrix composites with bimodal-sized B_4C reinforcement

Mohammad Raei, *Masoud Panjepour*, *and Mahmood Meratian*

Department of Materials Engineering, Isfahan University of Technology, Isfahan 84156-83111, Iran
(Received: 27 October 2015; revised: 2 March 2016; accepted: 7 March 2016)

Abstract: A new method was applied to produce an Al–0.5wt%Ti–0.3wt%Zr/5vol%B_4C composite via stir casting with the aim of characterizing the microstructure of the resulting composite. For the production of the composite, large B_4C particles (larger than 75 μm) with no pre-heating were added to the stirred melt. Reflected-light microscopy, X-ray diffraction, scanning electron microscopy, field-emission scanning electron microscopy, laser particle size analysis, and image analysis using the Clemex software were performed on the cast samples for microstructural analysis and phase detection. The results revealed that as a consequence of thermal shock, B_4C particle breakage occurred in the melt. The mechanism proposed for this phenomenon is that the exerted thermal shock in combination with the low thermal shock resistance of B_4C and large size of the added B_4C particles were the three key parameters responsible for B_4C particle breakage. This breakage introduced small particles with sizes less than 10 μm and with no contamination on their surfaces into the melt. The mean particle distance measured via image analysis was approximately 60 μm. The coefficient of variation index, which was used as a measure of particle distribution homogeneity, showed some variations, indicating a relatively homogeneous distribution.

Keywords: metal matrix composites; particle-reinforced composites; boron carbide; casting; thermal shock

1. Introduction

Because of better physical and mechanical properties of particulate-reinforced aluminum-matrix composites (PRAMCs) compared to monolithic alloy matrices, they [1–9] exhibit relatively higher performance in industrial applications. On the basis of the manner in which particles are introduced into the matrix, PRAMC manufacturing methods can be divided into two broad categories of *in situ* and *ex situ* methods. The advantages of *in situ* processes over *ex situ* processes are as follows: (1) *in situ* formation of reinforcements makes resulting composites thermodynamically stable in the matrix, which, in turn, results in less reduction in high-temperature properties; (2) *in situ* formation results in strong interfacial bonding as a consequence of clean reinforcement–matrix interfaces; and (3) *in situ* formation results in better mechanical properties because of a finer size and more uniform distribution of the *in-situ*-formed reinforcement particles in the matrix [10]. However, *in situ* processes also suffer some drawbacks: unwanted reaction products tend to form; the composition and nature of the reinforcement produced because of thermodynamic restrictions are governed by the phase diagram of any given system; and kinetic restrictions of chemical reactions leading to the formation of *in situ* reinforcement limit the shape, size, and volume fraction of reinforcements [11].

In addition to the positive aspects of the *ex situ* processes, which include simplicity and cost-effectiveness, one of the main problems encountered in the production of PRAMCs by *ex situ* processes such as stir casting is reinforcement agglomeration [12]. This problem becomes more severe with decreasing particle size. In the case of the Al–B_4C composite system, the homogeneous distribution of fine B_4C particles with a size under 10 μm in the microstructure has been demonstrated to become impossible via the casting method because of agglomeration [13].

According to the aforementioned arguments, a new *ex situ* processing route is proposed in this research for the

Corresponding author: Mohammad Raei E-mail: m.raei@ma.iut.ac.ir

Al–0.5wt%Ti–0.3wt%Zr/5vol%B_4C composite system. We produced the aforementioned composite using this new process and evaluated its microstructure.

2. Experimental

In this study, the materials used for the preparation of the matrix alloy were Al and Al–Ti and Al–Zr master alloys. The chemical compositions of these materials are presented in Table 1. The X-ray diffraction (XRD) pattern of the as-received B_4C is presented in Fig. 1. Approximately 600 g of Al with 99.5wt% purity was melted under air atmosphere in an alumina crucible using a resistance furnace. After the sample melted, the temperature reached 800°C; Al–10wt% Ti and Al–15wt% Zr master alloys were then added to the Al melt in the necessary amount for a nominal chemical composition of Al–0.5wt%Ti–0.3wt%Zr. The melt was maintained at 800°C for 40 min to dissolve the alloying elements. At this step, the Al melt containing the dissolved Ti and Zr was stirred at 700 r/min and 5vol% of B_4C with particle sizes larger than 75 μm were added to the melt at a rate of 1vol%/min. As shown in Fig. 2, the stirrer used for mixing had four vertical blades, each with a height and length of 3 and 2 cm, respectively. The B_4C particles were added at room temperature without any preheating. In fact, the large size of the B_4C particles and lack of preheating before their addition to the stirring melt were two key factors in the process. After this step, melt stirring was continued for another 10 min. Finally, the Al–0.5wt%Ti–0.3wt%Zr/5vol%B_4C composites were poured into a cylindrical steel mold with a height and diameter of 200 and 40 mm, respectively.

Table 1. Chemical composition of Al and the Al–Ti and Al–Zr master alloys wt%

Material	Al	Si	Fe	Cu	Zn	Cr	Ni	V	Ti	Zr
Aluminum	99.5	0.06	0.16	0.10	0.01	0.01	0.04	—	—	—
Al–Ti master alloy	Balance	0.09	0.19	—	—	—	—	0.02	10.5	—
Al–Zr master alloy	Balance	0.06	0.17	—	—	—	—	—	—	15 (14.3–15.7)

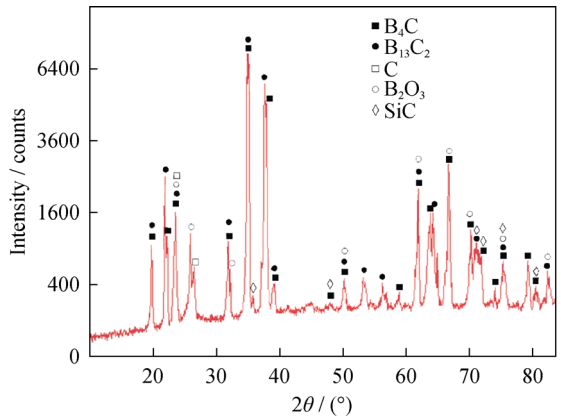

Fig. 1. XRD pattern of the as-received B_4C particles.

XRD was performed on the cast composite to qualitatively identify the presence of B_4C particles in the matrix. Reflected-light microscopy (RLM), scanning electron microscopy (SEM), and field-emission scanning electron microscopy (FESEM) were used to characterize the microstructure of the polished surface (I) of the cast composites, as shown in Fig. 3. Image analysis of the central part of this section was performed using the Clemex software. In addition, to evaluate the particle size distribution, the cast composite was dissolved in HCl acid and laser particle size analysis (LPSA) was used to grade the obtained B_4C particles. LPSA was also performed on the added B_4C particles.

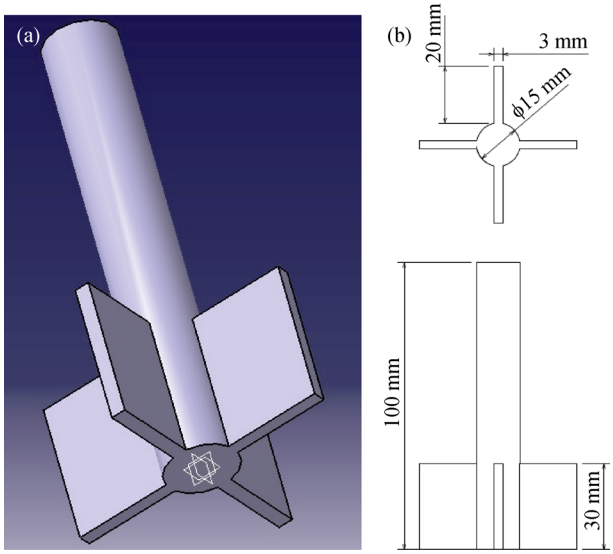

Fig. 2. Schematic shape of the stirrer used (a) and its related dimensions (b).

3. Results and discussion

3.1. Reinforcement incorporation evaluation

The XRD pattern of the stir-cast Al–0.5wt%Ti–0.3wt%Zr/5vol%B_4C composite is presented in Fig. 4. The B_4C and Al peaks detected in the pattern qualitatively indi-

cate that reinforcement incorporation occurred in the Al matrix. In general, the XRD pattern shows that the Al–0.5wt%Ti–0.3wt%Zr/5vol%B_4C composite can be successfully produced to some extent. However, for quantitative evaluation of the B_4C incorporated into the Al matrix, we analyzed FESEM images of the cast Al–0.5wt%Ti–0.3wt%Zr/5vol%B_4C composite microstructure. The FESEM images in the backscattered mode with the related Clemexed images are depicted in Fig. 5. In the figure, the dark particles in the matrix and the blue particles are B_4C particles. The image analysis results indicate that approximately 4.7vol% ± 0.1vol% B_4C particles are present in the matrix (4.6vol% and 4.8vol% B_4C particles in Figs. 5(a) and 5(b), respectively). On the basis of the amount of B_4C particles added (i.e., 5vol%, as mentioned in part 2), approximately all of the added particles were incorporated into the Al matrix during stirring. This high incorporation rate indicates that the stirring conditions related to stirrer shape, stirrer dimensions, stirring time, and stirring speed were appropriately chosen.

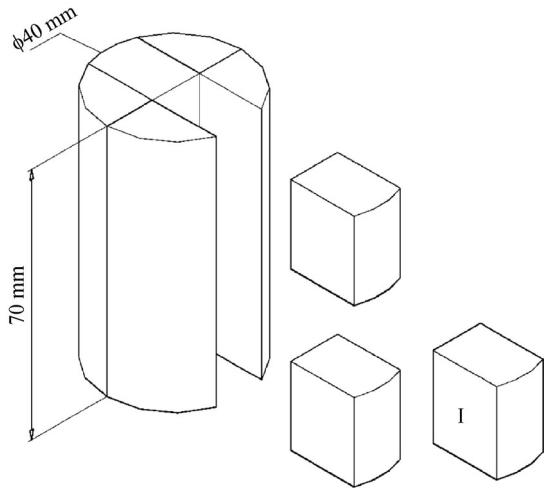

Fig. 3. Surface (I) extracted from the lower part of the cylindrical cast composite for metallography.

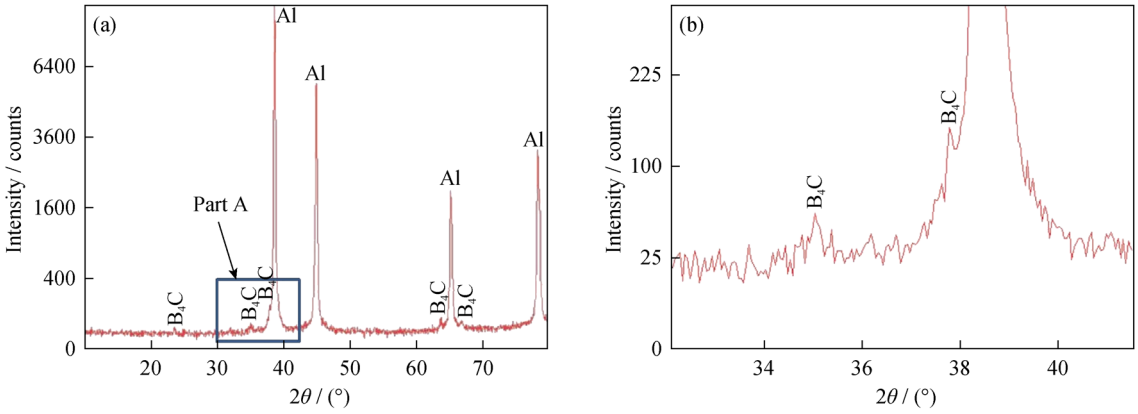

Fig. 4. XRD patterns of the Al–0.5wt%Ti–0.3wt%Zr/5vol%B_4C composite (a) and a detailed view of part A (b).

3.2. Reinforcement size and spatial distribution evaluation

SEM images of the cast composite microstructure are shown in Fig. 6. In addition to the large B_4C particles added to the cast composite during manufacture, fine particles with a size less than 75 μm are also observed. The LPSA results for the B_4C particles of the dissolved cast composite as well as those for the added B_4C particles are shown in Fig. 7. As evident in Fig. 7(a), the peak associated with the added B_4C particles is more intense than the peak of the B_4C particles obtained from dissolution. However, in the case of the curve of the B_4C particles obtained from dissolution, one peak at a size of approximately 16 μm is detected that was not observed in the curve of the added B_4C particles. The presence of this peak caused the accumulative curve of the B_4C particles obtained from dissolution to shift completely to the left of the curve of the added B_4C particles, as shown in Fig. 7(b). Approximately 18 vol % of the B_4C particles are less than 75 μm in size. These particles were not added to the cast composite externally; they were generated during the fabrication process. Accordingly, we concluded that the added particles experience a breakage during the process of fabricating this composite. This breakage leads to a reduction in the height of the peak associated with the B_4C particles obtained from dissolution (i.e., fewer large particles) and creates a peak at approximately 16 μm. On the basis of the SEM and LPSA results, we concluded that, although the added particles are larger than 75 μm, the fabricated composite enjoys bimodal sized particles.

To evaluate the reinforcement distribution and measurement of the mean particle distance in the current cast composite, image analysis was performed on the central part of section (I), as shown in Fig. 8. In the first step of this analysis,

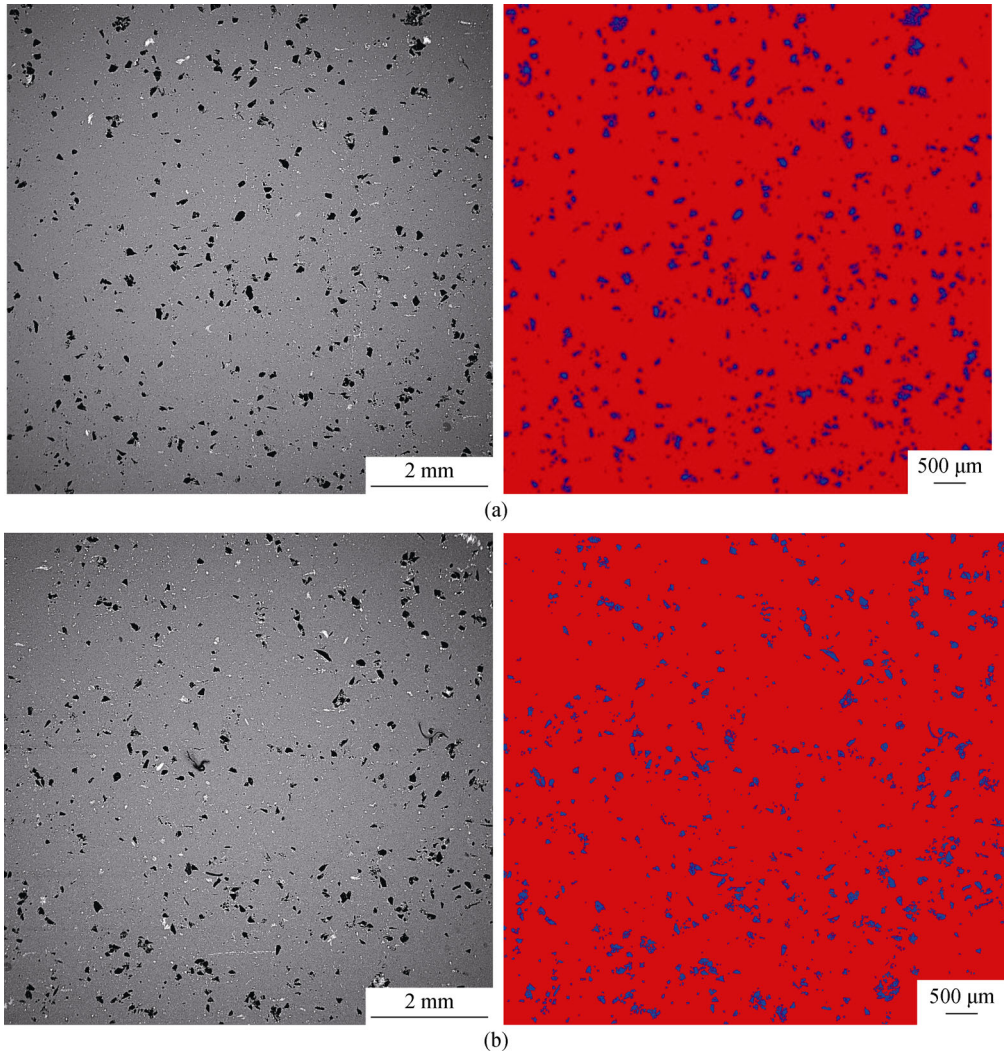

Fig. 5. FESEM images of the stir-cast aluminum–B_4C composite in a backscattered mode and the related Clemexed images: (a) 4.6vol% B_4C; (b) 4.8vol% B_4C.

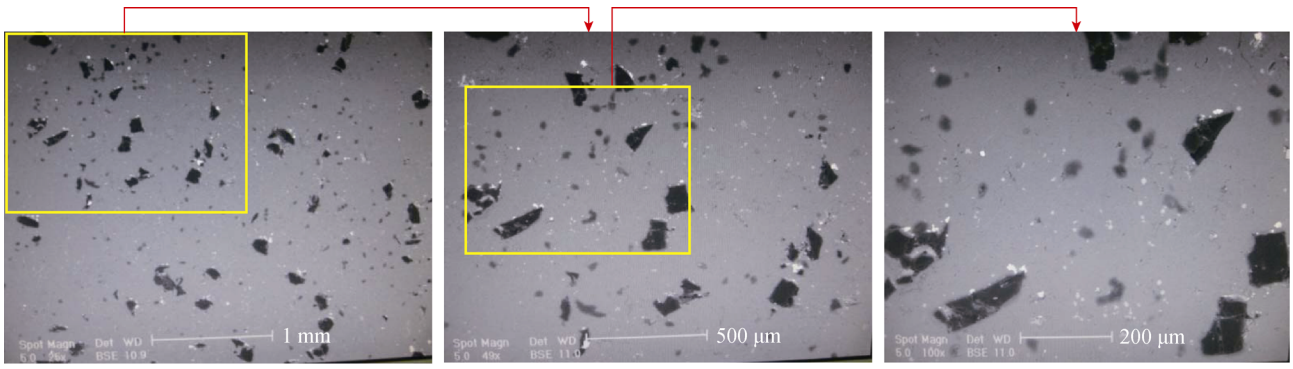

Fig. 6. SEM micrographs of the cast Al–0.5wt%Ti–0.3 wt%Zr/5vol%B_4C composite.

the central part of this section was divided into 36 parts, as depicted in Fig. 8. As shown in Fig. 9, in the second step of the image analysis, the particles in RLM images were identified and colored blue, whereas the matrix was colored red. Using the growth technique, we applied the tessellation method to the blue and red images. As shown in this figure, each cell was generated around one particle by this method (i.e., the center of each cell was the center of the related particle to that cell). Accordingly, the mean cell diameter was estimated as the mean particle distance.

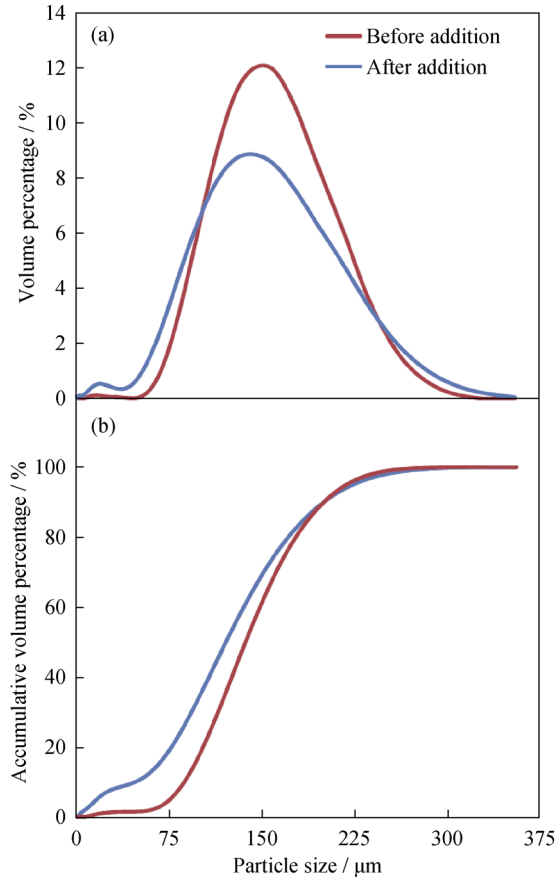

Fig. 7. Particle size distribution of the residual B_4C particles obtained from dissolution of the cast composite in hydrochloric acid and measured by the LPSA method: (a) volume percentage; (b) accumulative volume percentage.

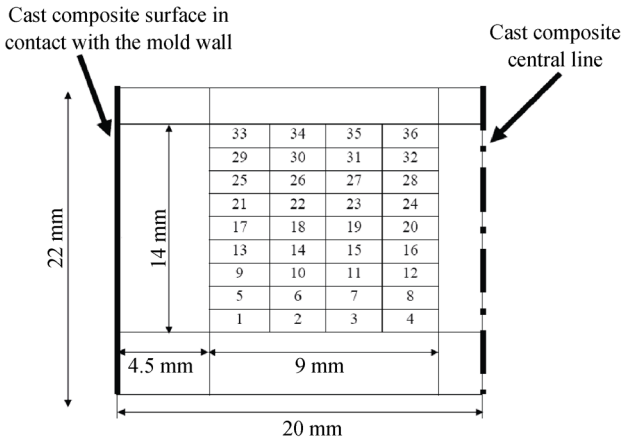

Fig. 8. Numbering of RLM images of surface (I) for image analysis.

The distribution of cell diameters on each RLM image indicated the homogeneity of particle distribution. Thus, for quantifying the homogeneity of particle distribution, the coefficient of variation (C.V.) was used. This parameter was calculated for a set of data (i.e., cell diameters on each RLM image) as Eq. (1) to provide a quantitative indication of data distribution. Eq. (1) is expressed as follows:

$$\text{Coefficient of variation (CV)} = \frac{\sigma}{\bar{x}} \qquad (1)$$

where σ and $\bar{x}$ are the standard deviation and the mean value for a given set of data, respectively. After applying the tessellation method to RLM images, we calculated the C.V. for each image on the basis of the size of the tessellated cells

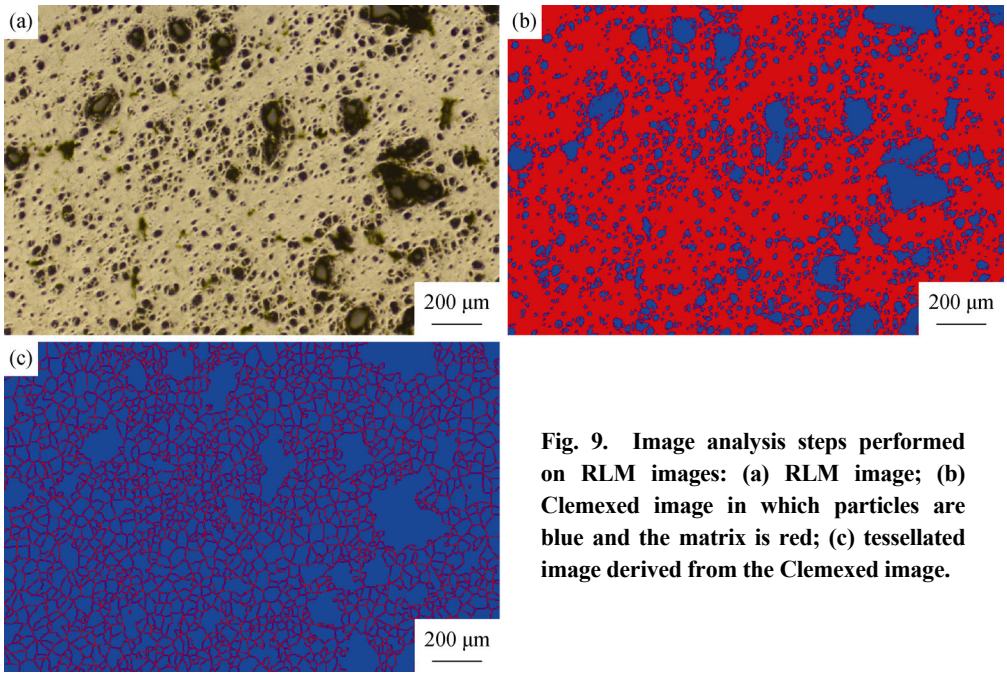

Fig. 9. Image analysis steps performed on RLM images: (a) RLM image; (b) Clemexed image in which particles are blue and the matrix is red; (c) tessellated image derived from the Clemexed image.

around each particle. These steps were performed on each of these 36 RLM images for three different conditions based on the particle size. In the first condition, only particles with a size greater than 75 μm were included in the image analysis; the smaller particles were omitted. Under the second condition, particles with a size less than 75 μm were included in the image analysis, and the larger ones were omitted. In the third condition, all of the particles were included in the image analysis.

The first result of this image analysis performed on the 36 RLM images is the mean particle distance for the three conditions, as shown in Fig. 10. As evident in the figure, the mean particle distance for the first condition (only large particles) was approximately 400 μm. The mean distance of the particles can be calculated by the following equation for a composite microstructure [14–15]:

$$\lambda = \sqrt{\frac{d^2}{V}} \tag{2}$$

where λ, d, and V are the particle mean distance, particle diameter, and particle volume percentage, respectively. By substituting 150 μm as the mean particle diameter d for the added B_4C particles and 0.05 for the particle volume percentage, we obtain a calculated particle mean distance of

$$\lambda = \sqrt{\frac{d^2}{V}} = \sqrt{\frac{150^2}{0.05}} \approx 670 \ \mu\text{m}.$$

This 670 μm is the particle mean distance under the assumption that the B_4C particles added to the system have not experienced any change and have retained their initial size.

We observed that the mean particle distance was reduced from 670 to 400 μm. This reduction indicates that the large-sized particles do not retain their initial size and are converted into smaller particles; however, they are still larger than 75 μm.

The average mean particle distance for the second condition (only small particles), as indicated in Fig. 10(b), is approximately 70 μm. One of the advantages of the presence of these fine B_4C particles is that λ is reduced dramatically and reaches approximately one-tenth of the calculated value, i.e., from 670 μm to approximately 70 μm. In the third condition (all particles), as depicted in Fig. 10(c), the average mean particle distance is approximately 60 μm. As expected, this value is less than the average mean particle distance for the other two conditions, which means that the composite with bimodal-sized particles has the lowest λ, the value of which is reduced from 670 μm (the calculated value) to 60 μm.

The second output of this image analysis performed on the 36 RLM images is the evaluation of the homogeneity of particle distribution. As a measure of the homogeneity of particle distribution, the CV was calculated for the 36 RLM images under the three aforementioned conditions; the results of these calculations are separately shown in Fig. 11 for each condition. The distribution homogeneity of large particles in the first condition is better than that in the two other conditions. The small particles are apparently not distributed as uniformly as the large ones. According to the CV results, the particles exhibit a relatively homogenous distribution in the composite as-cast microstructure in the 3rd condition (all particles), as indicated by the CV values

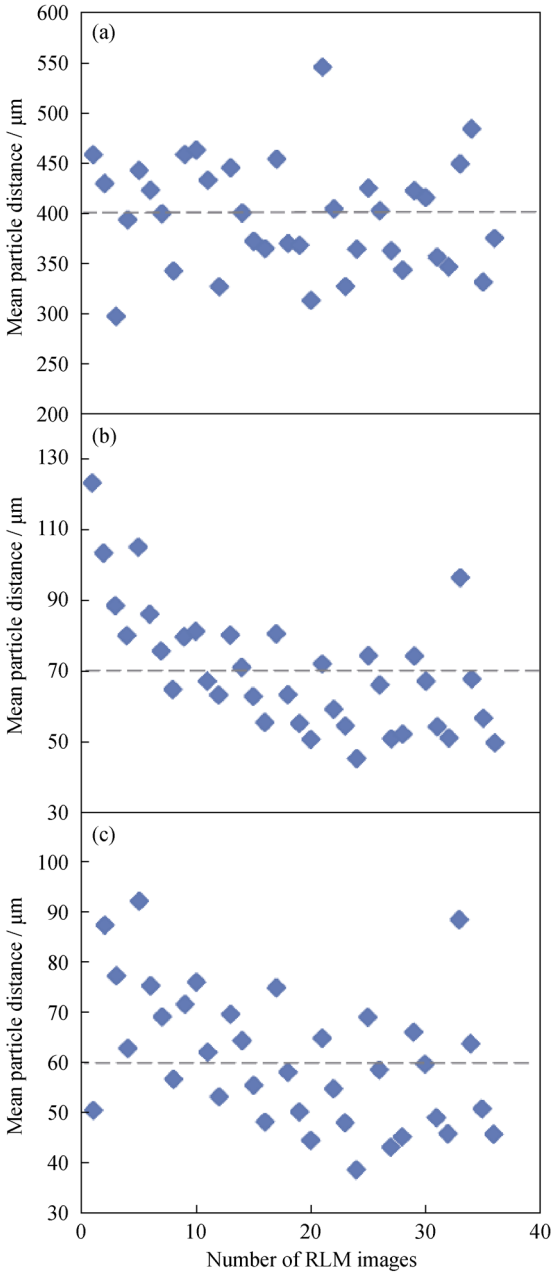

Fig. 10. Mean particle distance of only large particles (a), only small particles (b), and all particles (c).

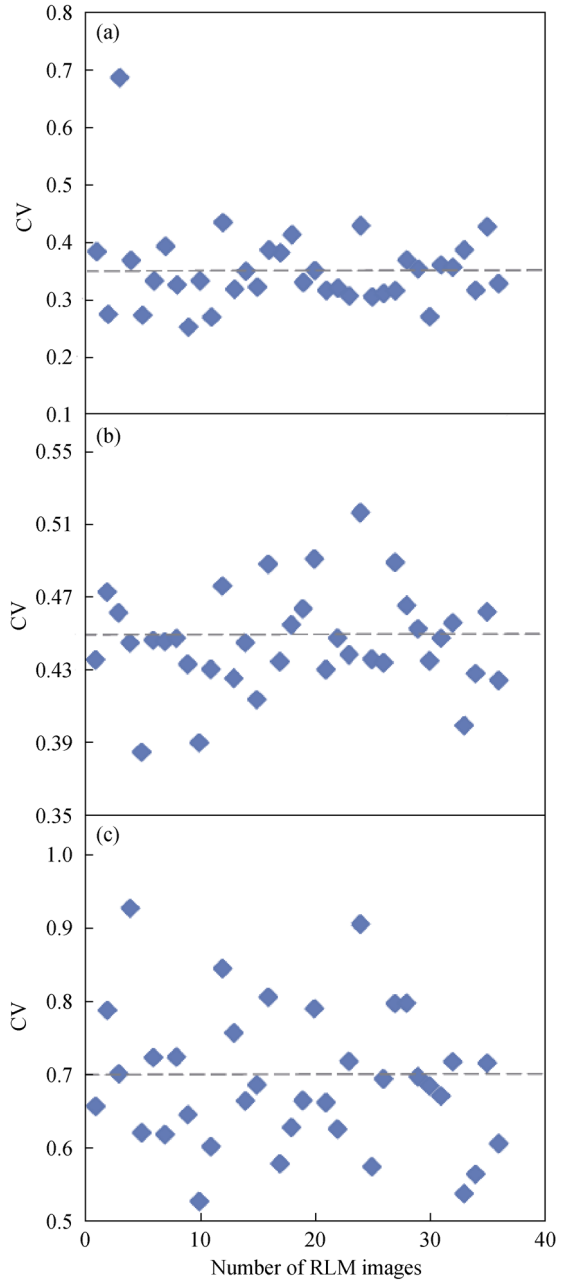

Fig. 11. Coefficient of variation (CV) as a measure of the distribution homogeneity for numbered RLM images of only large particles (a), only small particles (b), and all particles (c).

for different images being similar to each other. This slight variation in CV values is attributed primarily to the different distributions of fine B_4C particles in different parts of the Al matrix. According to the results obtained by Kerti and Toptan [13], the introduction of fine B_4C particles (<10 μm) into the Al matrix will cause the B_4C particles to agglomerate; hence, by the method used in this research, not only has the agglomeration problem of fine B_4C particles been solved, but a relative homogenous distribution of these fine particles has been achieved.

The size of the added B_4C particles was larger than 75 μm; hence, these fine particles were not externally added to the system. Some of the B_4C particles added to the composite system during fabrication experienced a two-step evolution. These two steps are as follows.

(1) Thermal shock exertion.

The addition of large B_4C particles to the Al melt at room temperature with no preheating subjects these ceramic particles to thermal shock. Failures generated by stresses exerted on the material because of sudden temperature changes are recognized as thermal shock [16]. For ductile materials such as metals and polymers, thermally induced stresses caused by thermal shock are alleviated by plastic deformation. By contrast, the brittleness of most ceramics does not permit plastic deformation in response to thermal stresses and hence increases the likelihood of brittle fracture in these materials [17]. Consequently, thermal stresses such as mechanical ones can lead to the fracture of brittle materials. Thermal shock behavior of a material is affected by its fundamental properties, including its coefficient of thermal expansion (CTE), modulus of elasticity, and fracture stress.

The resistance of a material to this kind of failure is termed thermal shock resistance and according to these parameters, it is approximated by the following equation:

$$R = \frac{\sigma_f (1-\upsilon)}{E\alpha} \tag{3}$$

where σ_f is the fracture stress of the material, υ is the Poisson's ratio, E is the modulus of elasticity, and α is the linear coefficient of thermal expansion [16].

Unlike the fundamental properties of ceramics with a given composition and microstructure (e.g., heat capacity, thermal conductivity, and thermal expansion), thermal shock resistance is a "derivative" behavior. Thermal shock resistance is affected by the fundamental properties of materials, by the imposed heat-transfer conditions, and by the geometry of the component experiencing thermal shock [18].

According to R data [19] for different ceramic materials, B_4C clearly exhibits a low thermal shock resistance (112°C); therefore, if the conditions are satisfied, it is prone to failure due to thermal shock. In the case of the processing conditions used in this research, the following two conditions caused the B_4C particles to break due to thermal shock: a large size of the added B_4C particles, and addition of the particles at room temperature without any preheating

Both of these parameters introduce a temperature gradient in the B_4C particles, which, in return, cause catastrophic failure. This temperature gradient was confirmed by simulation, as indicated in Fig. 12. In this 2D simulation, a circle-shaped B_4C particle was chosen. The surface tempera-

ture for this particle was set at 800°C, and an initial temperature of 25°C was applied. At the initial-time steps, a very sharp temperature gradient was present from the surface to the center of the B_4C particle, as shown in Fig. 13. This very large temperature gradient is the main cause of breakage for the brittle B_4C particle with a low thermal shock.

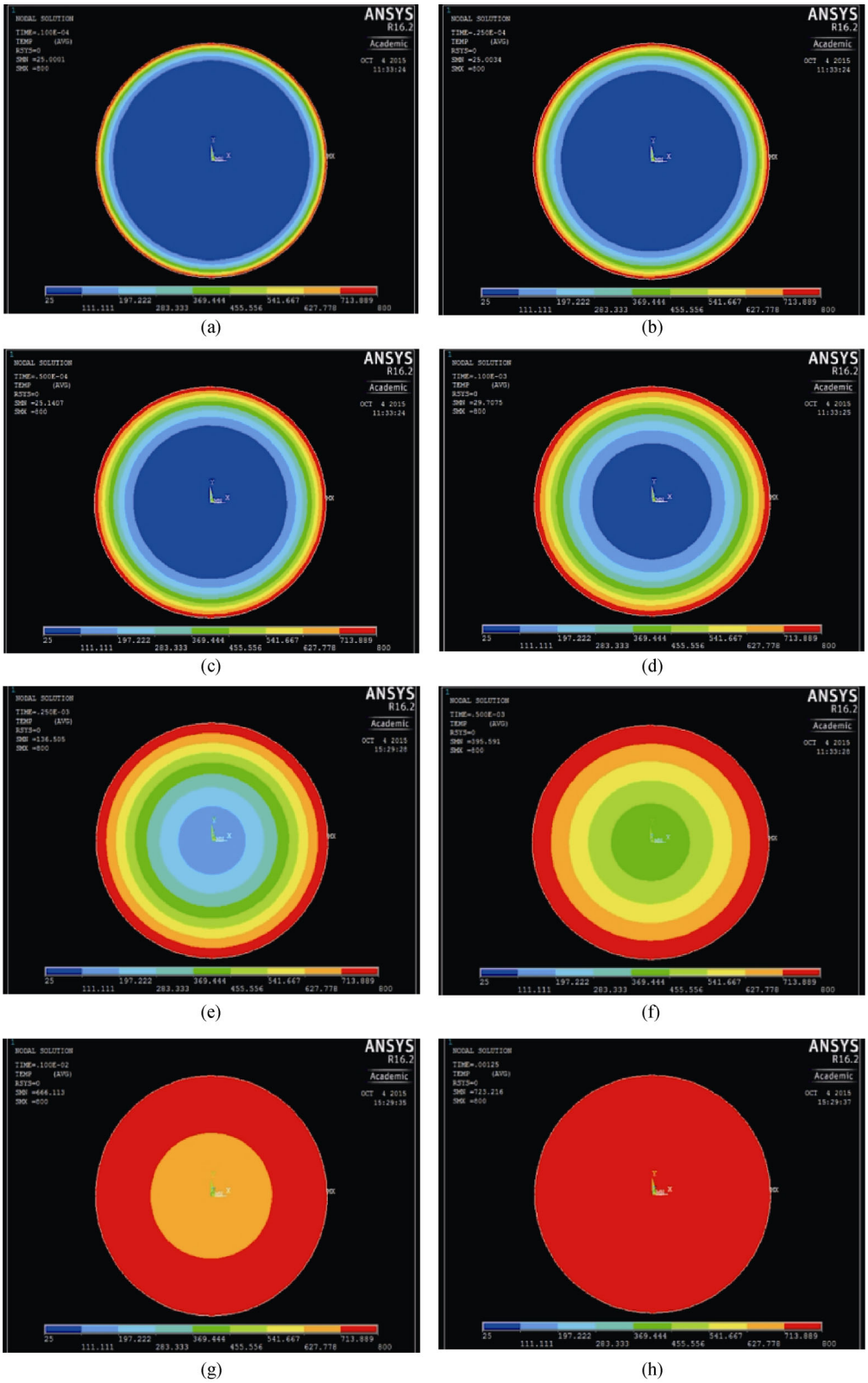

Fig. 12. Temperature gradient in a circle-shaped B_4C particle obtained by Ansys simulation at different time periods: (a) 10 μs; (b) 25 μs; (c) 50 μs; (d) 100 μs; (e) 250 μs; (f) 500 μs; (g) 1000 μs; (h) 1250 μs.

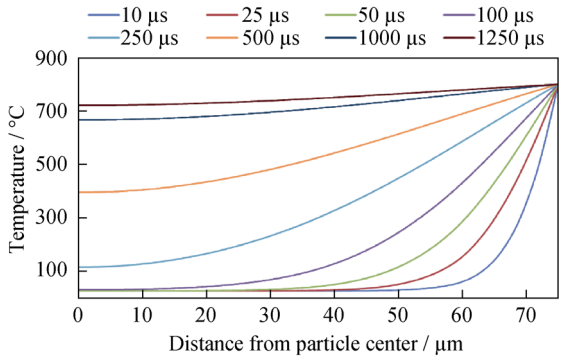

Fig. 13. Temperature gradient curves in a circle-shaped B_4C particle obtained by Ansys simulation versus distance from the particle center for different time steps.

Thus, these fine particles are clearly the product of the breakage of the large B_4C particles as a consequence of their low thermal shock resistance and the exertion of huge thermal shock. According to the low R value for alumina (77°C) given in Ref. [19], this ceramic material has the lowest thermal shock resistance; hence, this behavior is expected. In their research on cast Al–alumina composites, Pai *et al.* [20] reported such a phenomenon, but they did not take advantage of it. They mentioned thermal shock as one of the causes for alumina particle breakage.

(2) Creation of new fine particles with clean surfaces.

The most valuable effect of this B_4C particle breakage is the creation of fine particles with clean surfaces without any contamination. The clean, uncontaminated surface of these newly generated fine B_4C particles is another reason for the high incorporation of B_4C reinforcement during fabrication.

4. Conclusions

(1) Pseudo-*in-situ* was proposed as a new method for the production of stir-cast Al-matrix composites. In this method, B_4C reinforcements with a large particle size (over 75 μm) and low thermal shock resistance were introduced into the melt under an air atmosphere and at room temperature without any preheating. The addition of large B_4C particles at room temperature without any preheating subjected these particles to thermal shock. This thermal shock, the low thermal shock resistance of B_4C as a ceramic material and the large size of the added B_4C particles were the three key parameters responsible for the breakage of the B_4C particles.

(2) The mechanism of particle breakage due to the applied thermal shock involved two steps. In the first step, the thermal shock caused the breakage of the large B_4C particles into fine particles. In the second step, the clean, uncontaminated surfaces of the newly generated fine B_4C particles inducing high wettability were incorporated into the Al melt with the aid of stirring.

(3) This new processing route enabled exploitation of some of the most important *in situ* advantages through a simple and inexpensive *ex situ* method while simultaneously excluding some of its main drawbacks, such as the formation of unwanted reaction products and thermodynamic or kinetic limitations in the selection of elements.

(4) With this new method, the mean particle distance in the broken state decreased to approximately one-tenth its calculated value in the unbroken state (i.e., from 670 μm to approximately 60 μm) because of thermal shock.

(5) The distribution of the fine B_4C particles was relatively homogeneous in the matrix, with no agglomeration or clustering of these fine particles.

References

[1] S. Naher, D. Brabazon, and L. Looney, Simulation of the stir casting process, *J. Mater. Process. Technol.*, 143-144(2003), p. 567.

[2] K.R. Ravi, V.M. Sreekumar, R.M. Pillai, C. Mahato, K.R. Amaranathan, R. Arul kumar, and B.C. Pai, Optimization of mixing parameters through a water model for metal matrix composites synthesis, *Mater. Des.*, 28(2007), No. 3, p. 871.

[3] T. Sornakumar and M. Kathiresan, Machining studies of die cast aluminum alloy–silicon carbide composites, *Int. J. Miner. Metall. Mater.*, 17(2010), No. 5, p. 648.

[4] H. Su, W.L. Gao, H. Zhang, H.B. Liu, J. Lu, and Z. Lu, Optimization of stirring parameters through numerical simulation for the preparation of aluminum matrix composite by stir casting process, *J. Manuf. Sci. Eng.*, 132(2010), No. 6, art. No. 061007.

[5] P. Shanmughasundaram and R. Subramanian, Influence of magnesium and stirrer model in production of Al–fly ash composites: a Taguchi approach, *J. Appl. Sci. Res.*, 8(2012), No. 3, p. 1646.

[6] P. Ravindran, K. Manisekar, R. Narayanasamy, and P. Narayanasamy, Tribological behaviour of powder metallurgy-processed aluminium hybrid composites with the addition of graphite solid lubricant, *Ceram. Int.*, 39(2013), No. 2, p. 1169.

[7] M. Sameezadeh, H. Farhangi, and M. Emamy, Structural characterization of AA 2024–$MoSi_2$ nanocomposite powders produced by mechanical milling, *Int. J. Miner. Metall. Mater.*, 20(2013), No. 3, p. 298.

[8] M. Mohammadpour, R. Azari Khosroshahi, R. Taherzadeh Mousavian, and D. Brabazon, Effect of interfacial-active elements addition on the incorporation of micron-sized SiC particles in molten pure aluminum, *Ceram. Int.*, 40(2014), No. 6, p. 8323.

[9] Y.Q. Han, L.H. Ben, J.J. Yao, and C.J. Wu, Microstructural characterization of Cu/Al composites and effect of cooling

rate at the Cu/Al interfacial region, *Int. J. Miner. Metall. Mater.*, 22(2015), No. 1, p. 94.

[10] S.C. Tjong and Z.Y. Ma, Microstructural and mechanical characteristics of *in situ* metal matrix composites, *Mater. Sci. Eng. R Rep.*, 29(2000), No. 3-4, p. 49.

[11] R. Asthana, Solidification processing of reinforced metals: fabrication techniques, *Key Eng. Mater.*, 151-152(1998), p. 6

[12] I.A. Ibrahim, F.A. Mohamed, and E.J. Lavernia, Particulate reinforced metal matrix composites: a review, *J. Mater. Sci.*, 26(1991), No. 5, p. 1137.

[13] I. Kerti and F. Toptan, Microstructural variations in cast B_4C-reinforced aluminium matrix composites (AMCs), *Mater. Lett.*, 62(2008), No.8-9, p. 1215.

[14] J.J. Stephens, J.P. Lucas, and F.M. Hosking, Cast Al–7 Si composites: Effect of particle type and size on mechanical properties, *Scripta Metall.*, 22(1988), No. 8, p. 1307.

[15] J.P. Lucas, J.J. Stephens, and F.A. Greulich, The effect of reinforcement stability on composition redistribution in cast aluminum metal matrix composites, *Mater. Sci. Eng. A*, 131(1991), No. 2, p. 221.

[16] D.R. Askeland, P.P. Fulay, and W.J. Wright, *The Science and Engineering of Materials*, 6th Ed., Cengage Learning, Stamford, 2011.

[17] J. William D. Callister, *Fundamentals of Materials Science and Engineering*, 5th Ed., John Wiley & Sons, Inc., New York, 2001.

[18] G.T. Murray, *Handbook of Materials Selection for Engineering Applications*, Marcel Dekker, Inc., New York, 1997.

[19] M. Bengisu, *Engineering Ceramics*, Springer, New York, 2001.

[20] B.C. Pai, S. Ray, K.V. Prabhakar, and P.K. Rohatgi, Fabrication of aluminium–alumina (magnesia) particulate composites in foundries using magnesium additions to the melts, *Mater. Sci. Eng.*, 24(1976), No. 1, p. 31.